MATERIALS SCIENCE

Undulatory topographical waves for flow-induced foulant sweeping

Hangil Ko[1]*, Hyun-Ha Park[1]*, Hyeokjun Byeon[2], Minsu Kang[1], Jaeha Ryu[3], Hyung Jin Sung[3], Sang Joon Lee[2†], Hoon Eui Jeong[1†]

Diverse bioinspired antifouling strategies have demonstrated effective fouling-resistant properties with good biocompatibility, sustainability, and long-term activity. However, previous studies on bioinspired antifouling materials have mainly focused on material aspects or static architectures of nature without serious consideration of kinetic topographies or dynamic motion. Here, we propose a magnetically responsive multilayered composite that can generate coordinated, undulatory topographical waves with controlled length and time scales as a new class of dynamic antifouling materials. The undulatory surface waves of the dynamic composite induce local and global vortices near the material surface and thereby sweep away foulants from the surface, fundamentally inhibiting their initial attachment. As a result, the dynamic composite material with undulating topographical waves provides an effective means for efficient suppression of biofilm formation without surface modification with chemical moieties or nanoscale architectures.

INTRODUCTION

Natural living creatures often have remarkable fouling resistance that can effectively suppress surface contamination, which allows them to maintain pristine surfaces, while in direct contact with fluids containing diverse foulants including microorganisms. In contrast to synthetic antifouling materials such as biocides, silver, and nitric oxide that exhibit limited sustainable antifouling activities (*1*, *2*), natural antifouling materials are biocompatible, eco-friendly, and effective for a prolonged period of time (*3*). Inspired by nature, diverse materials that can prevent surface fouling while exhibiting biocompatibility and long-term activity have been developed. For example, membrane-mimicking zwitterionic monomer of 2-methacryloyloxyethyl phosphorylcholine (MPC) (*4*), lotus leaf– or dragonfly wing–mimicking superhydrophobic nanostructures (*5*, *6*), pitcher-inspired slippery liquid-infused surface (*7*), and shark skin–inspired micro-riblets (*8*) demonstrate pronounced antifouling and bactericidal properties in response to diverse microbial species without using toxic chemical substances. However, most previous studies on bioinspired antifouling materials have mainly focused on the material aspect or static micro- or nanoscale architectures of nature (*9*–*13*), without systematically considering dynamic topographies or motions of natural materials.

Living organisms and natural materials such as starfishes, sea urchins, mollusks, sea corals, seaweeds, mussel, the skin of pilot whales, dermal denticles of Batoidea, bird feathers, red blood cells, endothelial cells of arteries, and blood vessels are able to resist fouling based on their particular architectures and actuating motion (*14*, *15*). Inspired by these dynamic topographies of nature, recent studies have demonstrated that artificial surfaces with actuating microscale wrinkles can effectively inhibit biofouling by removing adhered biofilm based on delamination induced by the bending energy of the actuating wrinkled surfaces (*16*). The dynamic motion of cilia has also been used to actively remove adhered contaminants (*17*). Among the two main biofilm-targeting strategies that include the removal of established biofilms and the prevention of initial bacterial attachment (*18*), these previous studies are associated with the former: removal of established biofilms. These bioinspired dynamic materials exhibited fouling-resistant characteristics that can lead to the development of more efficient and sustainable antifouling materials. However, despite the apparent potential, studies on dynamic antifouling materials are still in their infancy and require further development. In particular, studies on synthetic dynamic materials that can prevent biofilm formation based on the generation of surrounding fluid flow have rarely been explored (*19*).

Here, we propose a new fouling-resistant strategy inspired by the dynamic undulatory topographical motion of Batoidea. This bioinspired artificial material was designed to exhibit coordinated dynamic sinusoidal topographical waves, for which characteristic length and time scales can be controlled on the basis of a magnetoresponsive, multilayered dynamic undulatory composite. Unlike previous studies that exploited the delamination mechanism of already developed biofilms, this dynamic composite sweeps foulants and fundamentally prevents initial foulant attachment with the aid of local and global fluid flow induced by the dynamic topographical waves. Because it is very difficult to remove mature biofilms once they are established (*20*), dynamic composites that can sweep away foulants and inhibit initial foulant adhesion might provide an efficient pathway to the development of sustainable bioinspired antifouling materials.

RESULTS

Design of the responsive dynamic undulatory composite

Batoidea undergoes front-to-rear undulatory motions in its planar body to generate momentum for aquatic propulsion by actuating the pectoral fins of a multilayered musculoskeletal structure (Fig. 1A) (*21*). This coordinated undulatory gait induces vortices around the body (Fig. 1B) (*21*, *22*), which was conjectured in our design of a dynamic undulatory composite to sweep foulants with the objective

[1]Department of Mechanical Engineering, Ulsan National Institute of Science and Technology (UNIST), Ulsan 44919, Republic of Korea. [2]Department of Mechanical Engineering, Pohang University of Science and Technology, Pohang 37673, Republic of Korea. [3]Department of Mechanical Engineering, Korea Advanced Institute of Science and Technology (KAIST), Daejeon 34141, Republic of Korea.
*These authors contributed equally to this work.
†Corresponding author. Email: sjlee@postech.ac.kr (S.J.L.); hoonejeong@unist.ac.kr (H.E.J.)

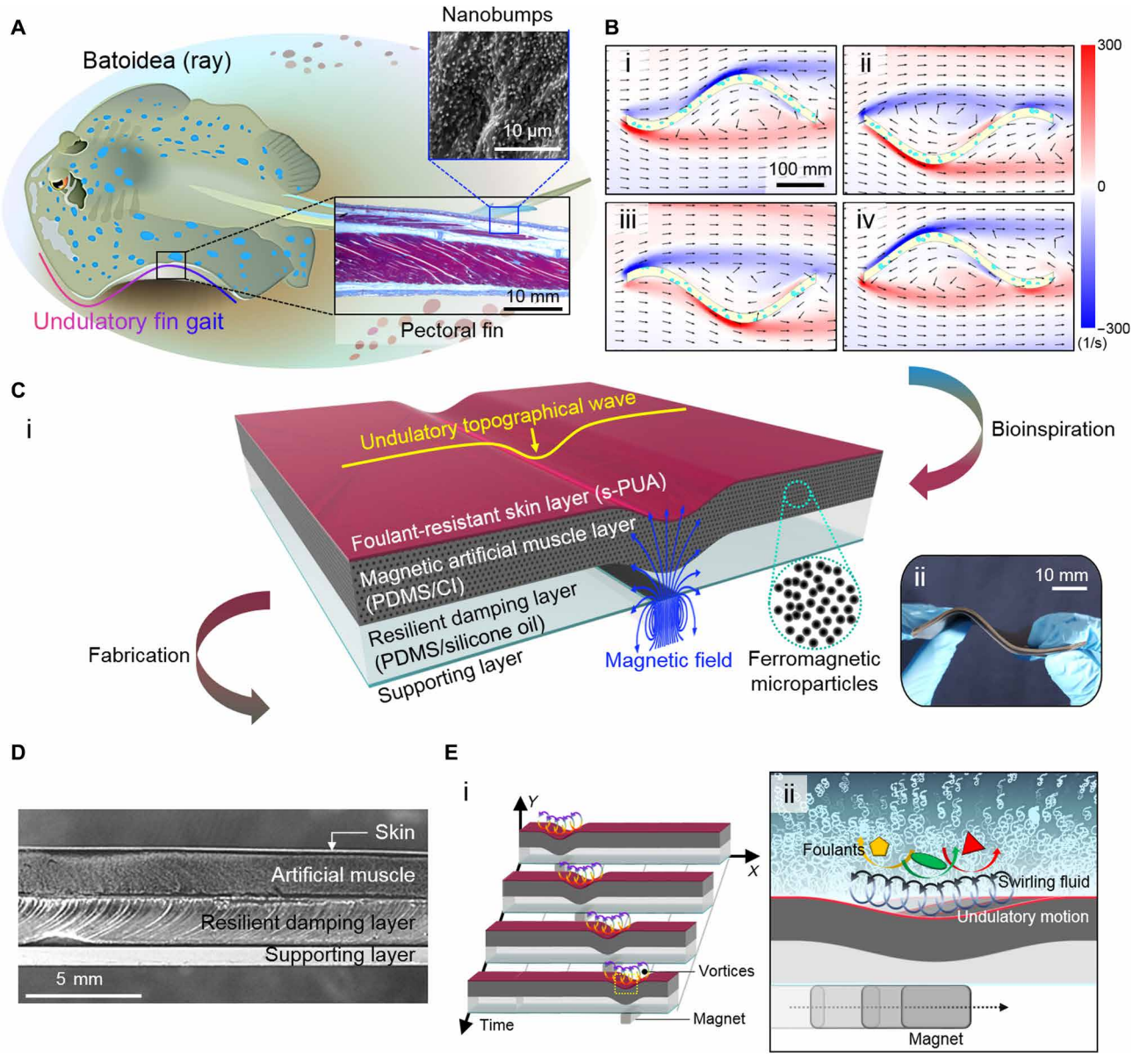

Fig. 1. Design of the Batoidea-inspired dynamic undulatory composite. (**A**) Conceptual illustration showing the undulatory gait of the Batoidea's pectoral fin together with the histological cross section of the pectoral fin (red, muscle; blue, collagen and bone). Nanoscale bumps are observed on the surface of the pectoral fin (scanning electron microscopy image). (**B**) Schematic illustrations showing vortices around the pectoral fin induced by the undulatory gait. (**C**) (i) A schematic structure of the multilayered dynamic undulatory composite and (ii) image of the fabricated composite. (**D**) A cross-sectional stereo zoom microscope image of the fabricated multilayered undulatory composite. (**E**) Schematic illustrations showing (i) the propagating undulatory topographical wave along with the translation of the magnet and (ii) the topographical wave–induced sweeping of foulants.

of preventing surface fouling. The dynamic undulatory composite proposed in this study consisted of four layers: the uppermost skin, an intermediate artificial muscle, an underlying resilient damper, and bottom support (Fig. 1C, i). The upper skin is a flexible passivation layer of the dynamic composite with a thickness of 100 μm. It was made of soft polyurethane acrylate (s-PUA). The s-PUA was used for the skin layer because of its rapid ultraviolet (UV)–curable property, tunable surface energy, and flexibility (*23*). In addition, functional moieties or nanostructures can be realized over the s-PUA skin layer with the aid of its acrylate group and UV-patternable property. The artificial muscle layer (AML) is composed of polydimethylsiloxane (PDMS) embedded with ferromagnetic carbonyl iron (CI) microparticles (diameter, 1 to 5 μm). This muscle layer can deform immediately in response to an externally applied magnetic field without complicated wired electrical or pneumatic connections. The resilient damping layer (RDL) was designed to have a low elastic modulus (~10 kPa) by using a PDMS/silicone oil mixture. Its damping allows depthwise deformations of the upper skin and muscle layers without any protrusion of the bottom side of the damping layer, while its resiliency enables the recovery of deformations. The most basal layer that acts as a supporting layer was made of flexible polyethylene terephthalate (PET) film or rigid glass. Macroscopically,

the fabricated dynamic composite was in the form of a highly flexible multilayered film (Fig. 1C, ii). Figure 1D shows the cross-sectional image of the fabricated composite, in which each thickness of the skin, muscle, damping, and supporting layers is 0.100, 2.0, 2.1, and 1.0 mm, respectively. The thickness of each layer can be modulated upon demand. When a magnetic field is applied to the composite, the skin layer conformally attached to the muscle layer deforms in the depth direction of the composite. Upon horizontal movement of the magnetic field, the depthwise deformation propagates along the direction of the field movement. This generates sinusoidal undulatory surface waves of the composite (Fig. 1E, i). These undulatory topographical waves would generate local or global vortices in the region near the composite surface, which could be harnessed for the suppression of surface fouling (Fig. 1E, ii).

Undulatory topographical waves of a dynamic undulatory composite

The deformation of a composite material in response to a magnetic field can be predicted by coupling a Maxwell stress tensor and a mechanical stress tensor (*24*, *25*). The electromagnetic stress tensor $\sigma_{EM,ij}$ for the magnetostatic condition is given by (see note S1 for details) (*26*)

$$\sigma_{EM,ij} = \frac{1}{\mu_0}\left(B_i B_j - \frac{1}{2}B^2\delta_{ij}\right) \quad (1)$$

where μ_0 is the magnetic constant, B is the magnetic field, and δ_{ij} is Kronecker's delta. According to the Hooke's law for isotropic materials, the strain ε_{ij} associated with the mechanical stress tensor $\sigma_{M,ij}$ is given by (*27*)

$$\varepsilon_{ij} = \frac{1}{E}(\sigma_{M,ij} - \nu(\sigma_{M,kk}\delta_{ij} - \sigma_{M,ij})) \quad (2)$$

where ν and E represent Poisson's ratio and Young's modulus, respectively. By coupling Eqs. 1 and 2 with a condition of $\nabla(\sigma_M + \sigma_{EM}) = 0$, Eq. 2 can be expressed as

$$\varepsilon_{ij} = -\frac{1}{E}(\sigma_{EM,ij} - \nu(\sigma_{EM,kk}\delta_{ij} - \sigma_{EM,ij})) \quad (3)$$

Figure 2 (A to C) shows the finite element analysis (FEA) results for the magnetic field density, Maxwell stress tensor, strain tensor, and corresponding displacement of the composite for three different RDL thicknesses (t_{RDL}: 0.7, 1.4, and 2.1 mm). The magnetic field density along the plane parallel to the magnet movement (plane 1) has a maximum value just above the magnet [Fig. 2, A (i) and B (i), and fig. S1]. Accordingly, a dimple is formed in the location of the dynamic composite just above the magnet. The FEA results also show that the degree of deformation can be modulated by adjusting the thickness of the RDL (t_{RDL}). A thicker RDL gives rise to a larger deformation of the composite, despite the increased distance to the magnet (Fig. 2, A to C, and fig. S1). This is mainly attributed to the following: (i) The AMLs of the composites with three different t_{RDL} (0.7, 1.4, and 2.1 mm) are all within the influence of the magnetic field. The differences in the magnetic field densities of the three composites with different t_{RDL} do not induce noticeable differences in their deformations. (ii) The depth of the deformation is mainly determined by the compressive stiffness (k) of the RDL. The k and deformation depth (δ) of the RDL can be given by

$$k = \frac{A \cdot E}{t_{RDL}} \quad (4)$$

$$\delta = \frac{\sigma \cdot A}{k} = \frac{\sigma \cdot t_{RDL}}{E} \quad (5)$$

where A and E represent the area and elastic modulus of the RDL, respectively. These equations indicate that a higher t_{RDL} leads to lower compressive stiffness k, allowing higher deformation δ under identical normal stress. In addition, a higher t_{RDL} implies that more deformable underlying layer is provided to the upper AML. This also contributes to a higher deformation of the thicker RDL. Figure 2D compares the experimental results (Fig. 2D, i) and the numerical simulation (Fig. 2D, ii) for the deformations of the composites with three different t_{RDL} values. The experimental results are in good agreement with the numerical predictions (Fig. 2E).

The directional modulation of the magnetic field facilitates the propagation of the topographical deformation of the composite in a predetermined direction. Figure 3A shows sequential monochromic cross-sectional images of the undulatory surface waves of the composite that were generated by the unidirectional translation of a permanent magnet. Initially, the integrated multilayered composite of the skin, magnetic muscle, and resilient damper just above the magnet undergoes a depthwise deformation (Fig. 3A, i). Because of the movement of the magnet, the deformation propagates along the horizontal direction, causing sinusoidal surface waves in the skin layer [Fig. 3A (ii to vii) and movie S1]. The amplitude and frequency of the undulatory waves can be readily regulated by varying the modulation of the external magnetic field or the thickness of the RDL. To investigate the topographical waves in further detail, rhodamine B was mixed with the s-PUA during the fabrication of the skin layer. Time-lapse fluorescence images of the skin layer dyed with rhodamine B show the dynamic undulatory topographical waves of the composite (Fig. 3B and movie S2). The experimentally observed topographical waves are in good agreement with the FEA results (fig. S2). It should be noted that the undulatory motion of the proposed dynamic composite differs from that of the cyclic wrinkling-flattening in that a single dimple propagates along a specific horizontal direction. Sinusoidal translational waves are generated in the dynamic composite (fig. S2), while multiple wrinkles are generated and disappeared simultaneously in actuating wrinkle-based materials (*16*, *20*).

Fluid flow induced by undulatory topographical waves

The undulatory surface waves of the composite could induce alterations in the fluid flow that is in contact with the surface due to fluid-structure interactions. To investigate the fluid dynamic characteristics on the dynamic composite surface that exhibits undulatory surface waves, we conducted particle image velocimetry (PIV) measurements of flow over the dynamic surface. For the PIV experiment, NaCl solution containing tracer microparticles (diameter, 20 to 50 μm) was supplied over the composite surface (thickness of the NaCl solution, 4 mm) (see Materials and Methods for details). Then, a spherical magnet was reciprocated along the x axis (Fig. 4A) with a speed of 20 mm s^{-1} with a one-way traveling distance of 30 mm. The deformation depth of the dimple was maintained at 0.394 mm during the PIV experiments. The PIV results show noticeable alterations in the velocity field of the flow, caused by the undulatory surface waves (Fig. 4B). Upon the initial depthwise deformation of the composite at $t = 0.1T$ (here, T represents the periodic time for the reciprocating motion of the dimple; fig. S3), a downward moving stream is generated with an enhanced flow velocity in the deformed region compared to that in the remaining nondeformed regions of

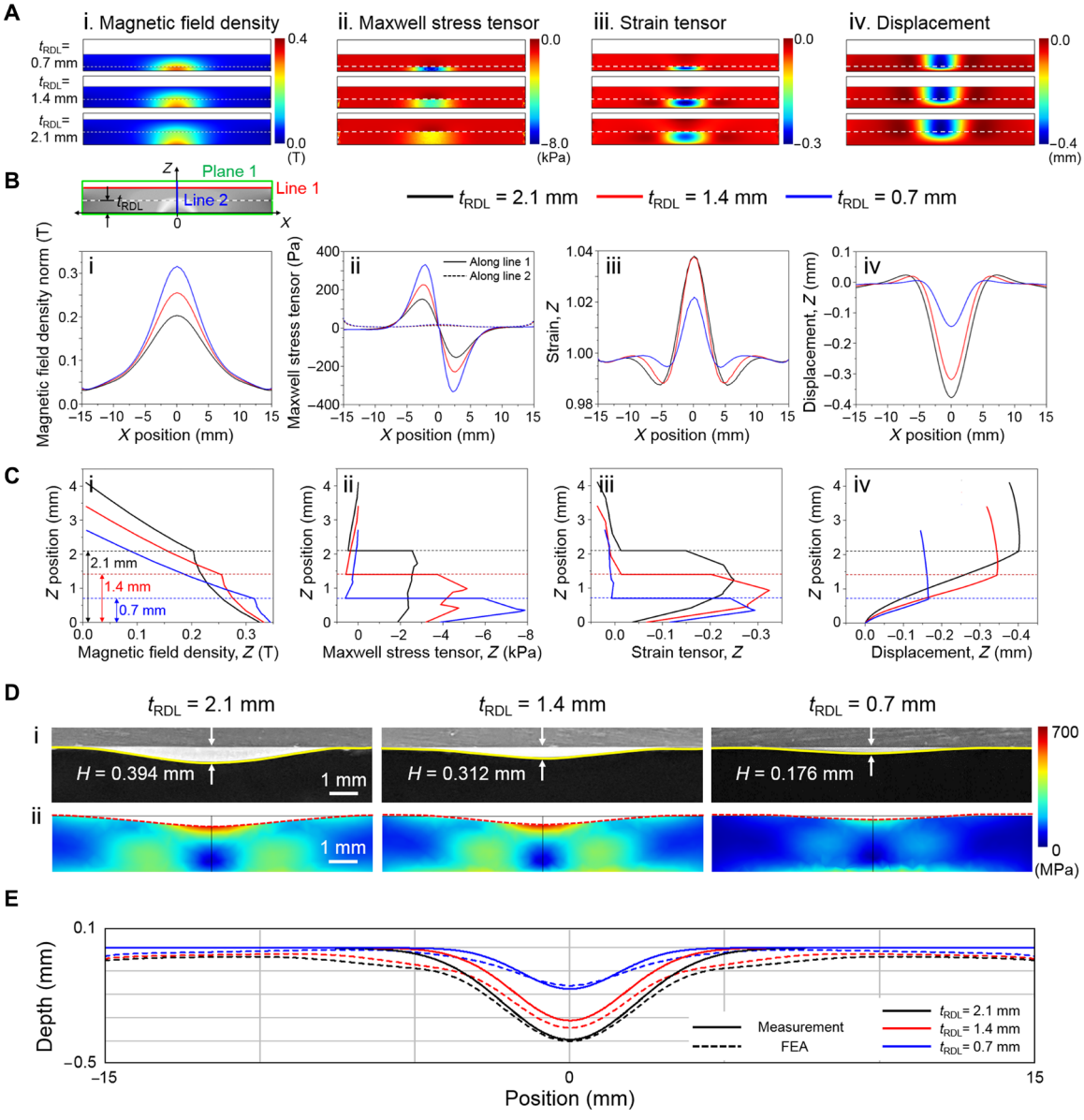

Fig. 2. Magnetic field–responsive deformations of the dynamic undulatory composite. (**A** to **C**) Quantitative FEA results of the magnetic field density, Maxwell stress tensor, strain tensor, and displacement of the composites with three different thicknesses of the RDL (t_{RDL}) along (A) plane 1 (the cross-sectional plane parallel to the magnet movement), (B) line 1 (top horizontal line of plane 1), and (C) line 2 (vertical center line of plane 1). Detailed descriptions of the plane and the lines of interests are available in fig. S1. (**D**) (i) Cross-sectional views and (ii) simulation results of the deformations of the composite with different values of t_{RDL} (2.1, 1.4, and 0.7 mm). (**E**) Comparisons of the experimental deformation behaviors of the composite with the FEA results.

the composite surface [Fig. 4B (i), $t = 0.1T$]. When the deformed dimple is moved along the x direction during the undulatory motion of the composite, the fluid above the newly generated dimples exhibits downward flow with enhanced velocity. However, the fluid in the regions where a previous dimple existed is subjected to a reversed, upward moving flow due to the elastic recovery of the composite surface [Fig. 4B (ii), $t = 0.2T$]. Accordingly, the consecutive propagation of dimple and sinusoidal surface waves leads to the generation of the vortex over the composite surface. Furthermore, reciprocating and repeating topographical waves result in local and global generation of the vortex over the composite surface along the x axis (plane 1 in Fig. 4B). Apart from the longitudinal plane (plane 1), notable velocity gradients are also observed in the transverse plane (plane 2 in Fig. 4B).

Theoretically, the fluid dynamics over the undulatory dynamic composite can be predicted from the coupling stress tensors of the fluid and solid domains. The fluid dynamics were analyzed using a two-way fluid-structure interaction approach. The Navier-Stokes equation and continuity equation for an incompressible fluid flow domain are given by (*28*, *29*)

$$\frac{\partial u_i}{\partial t} + u_j \frac{\partial u_i}{\partial x_j} = -\frac{1}{\rho^F}\frac{\partial p}{\partial x_i} + \nu \frac{\partial^2 u_i}{\partial x_j x_j} + f_i^F \quad (6)$$

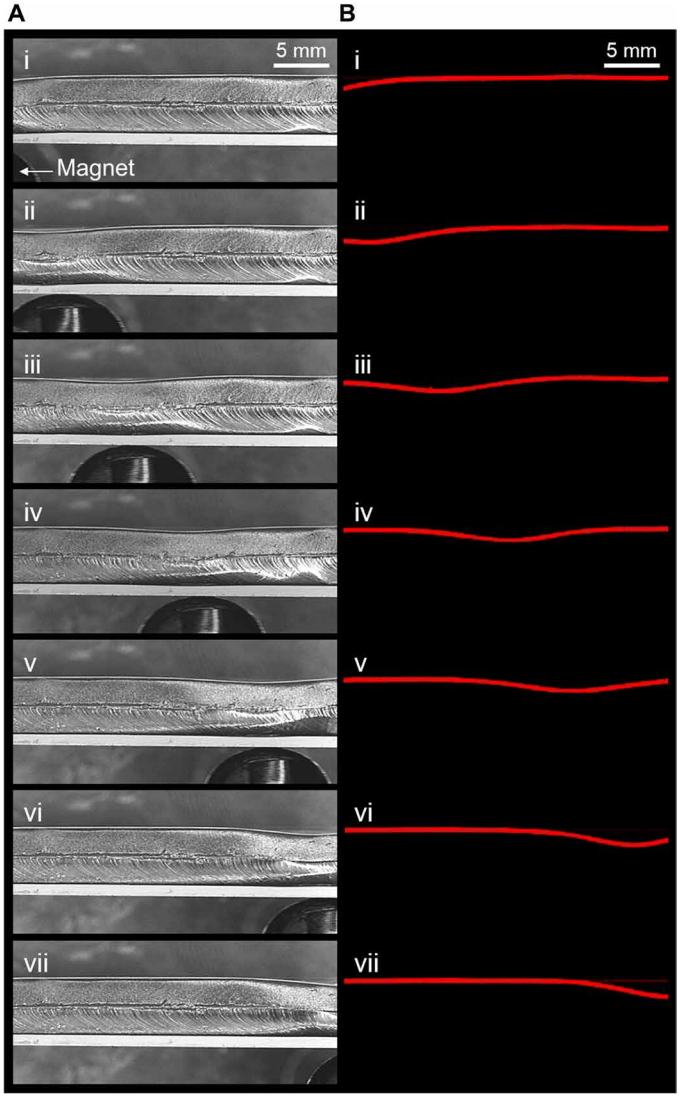

Fig. 3. Undulatory topographical waves of the dynamic composite modulated by the controlled magnetic field. (**A**) Time-lapse monochromic cross-sectional images of the undulatory surface waves of the composite generated by the translation of a permanent magnet. (**B**) Time-lapse fluorescence cross-sectional images of the undulatory surface waves of the composite. The skin layer of the composite was dyed with rhodamine B.

$$\frac{\partial u_i}{\partial x_i} = 0 \tag{7}$$

where u, ρ^F, p, ν, and f^F represent the velocity, density, pressure, kinematic viscosity of the fluid, and external volume force in the fluid domain, respectively. The equation for the stress tensor of a fluid is obtained by solving the nonlinear Navier-Stokes equation (*28*, *29*)

$$\sigma_{F,ij} = -p\delta_{ij} + \tau_{ij} = -p\delta_{ij} + \mu\left(\frac{u_i}{x_j} + \frac{u_j}{x_i}\right) \tag{8}$$

where μ and τ_{ij} represent the dynamic viscosity and deviatoric stress tensor, respectively.

In the solid domain, the continuity equation for a deformable solid surface is expressed by (*30*)

$$\rho^S \frac{D^2 h_i}{Dt^2} - \frac{\partial \sigma_{S,ij}}{\partial x_j} = \rho^S f_i^S \tag{9}$$

where ρ^S, h, $\sigma_{S,ij}$, and f^S represent the density, displacement, solid stress tensor, and external volume force in the solid domain, respectively. The equation of solid stress tensor is given by (*30*)

$$\sigma_{S,ij} = J^{-1} F \cdot S \cdot F^T \tag{10}$$

where F, S, and J signify the deformation gradient tensor, second Piola-Kirchhoff stress tensor, and Jacobian (determinant of F), respectively. The equation of the flow velocity field as a function of mechanical deformation can be solved by the arbitrary Lagrangian-Eulerian method based on the kinematic and dynamic coupling equations with proper boundary conditions (see note S2 for details) (*31*–*34*). FEA results of the fluid dynamics over the undulatory surface waves were obtained using COMSOL Multiphysics. As shown in fig. S4A, the numerical prediction results exhibit similar overall trends with the PIV results. The translational propagation of the dimple not only creates strong local vortices near the deformation site but also induces global vortices in the longitudinal plane, as illustrated by the streamlines in fig. S4A.

Figure 4C shows the periodical variation of three velocity components in the x (V_x), y (V_y), and z (V_z) directions along the center ($x = 0, y = 0, z = 0$) of the composite surface during the repeating five T cycles. Each centerline velocity component evaluated from the PIV results exhibits a periodic increase and decrease during the reciprocating motion of the dimple (Fig. 4C, i). The three mean velocity components, which were averaged for 10 reciprocating cycles, are illustrated in Fig. 4C (ii). Up to $t = 0.1T$, all velocity components have low values. It is attributed to the fact that the center is located far from the deformed site at $t = 0.1T$ [see Fig. 4B (i)]. However, at $t = 0.2T$, V_z remarkably increases to −1.34 mm s^{-1}. In this case, the negative velocity indicates the downward flow motion of the fluid. At $t = 0.3T$, the direction of V_z is reversed and the magnitude increases to 0.89 mm s^{-1}, followed by a decrease to 0 mm s^{-1} at $t = 0.5T$ (see Fig. 4B, iii and iv). In the periodic phase of $0.1T$ to $0.5T$, V_x also exhibits large fluctuations from 0.44 to −0.99 mm s^{-1}. These results indicate that there are notable velocity variations in the vertical z and longitudinal x directions when the undulatory waves propagate along the x direction. In contrast, V_y is nearly zero during the entire cycle. This indicates that the transverse velocity component, with respect to the wave propagation direction, is negligible. On the basis of the maximum velocity ($u \sim 1.5$ mm s^{-1}), characteristic length ($l \sim 4$ mm), and oscillatory period ($3 \text{ s} < t < 60$ s) of the surface wave–induced flow in the system, the Reynolds number ($Re = \rho ul/\mu$, where ρ is the fluid density and μ is the dynamic viscosity), Strouhal number ($St = l/tu$), and Froude number [$Fr = u/(lg)^{0.5}$, where g is the gravitational acceleration] are in the range of $Re < 6.7$, $0.04 < St < 0.89$, and $Fr < 7.57 \times 10^{-3}$, respectively (see note S3 for details).

To further examine the vortices generated on the undulatory surface, path lines along the longitudinal (plane 1) and transverse (plane 2) directions were investigated on the basis of the PIV measurements. As shown in Fig. 4D, numerous vortices are generated on the dynamic undulatory composite surface, as evidently demonstrated by the path lines of individual particles. The vortices are especially substantial in the region near the dynamic surface in the longitudinal plane (plane 1). In the transverse plane (plane 2), particles in the center of the plane exhibit up-and-down path lines, while particles

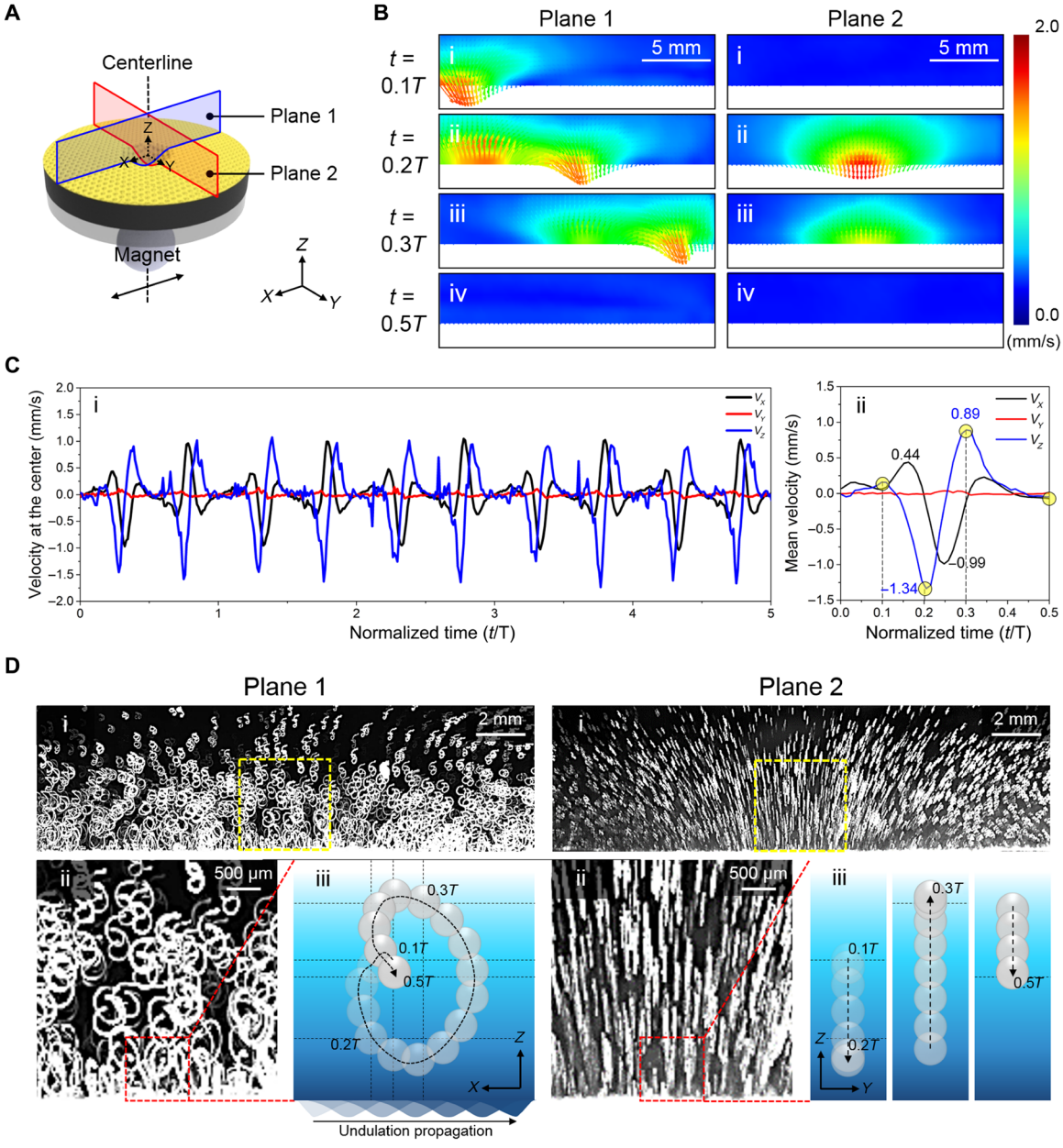

Fig. 4. Analysis of fluid flow on the dynamic undulatory composite. (**A**) Schematic diagram of the experimental setup and the planes of interest for the PIV experiment. (**B**) PIV measurement results for a flow on the dynamic undulatory surface observed along plane 1 and plane 2 as a function of the periodic time (t/T) of the topographical wave with $T = 3$ s and $H = 0.394$ mm. (**C**) (i) Variations of three velocity components of the flow in the x (V_x), y (V_y), and z (V_z) directions at the center ($x = 0, y = 0, z = 0$) of the undulatory surface during the repeating five T cycles, evaluated from the PIV results, and (ii) mean velocity components averaged from the experimental data during 10 reciprocating cycles. (**D**) (i and ii) Photographs showing the path lines of tracer particles and (iii) analyzed trajectories of single tracer particle on the undulatory surface along plane 1 (left) and plane 2 (right), which were obtained through PIV velocity field measurements with $T = 3$ s and $H = 0.394$ mm.

in the region out of the center exhibit rotational path lines. The FEA results on the vortices and path lines of particles on the dynamic composite surface are in good agreement with the experimental results showing strong vortices and swirling motions of individual particles on the surface (fig. S4B).

Sweeping of foulants and antifouling properties of the undulatory composite

The antifouling performance of the dynamic undulatory composite was examined by culturing *Escherichia coli* cells on the surface. Real-time optical images of bacterial movements and swimming traces on the dynamic surface and static control surface were connectively captured. It is well known that planktonic bacteria exhibit random behavioral patterns before they irreversibly adhere to solid surfaces and form mature biofilms (*20*). Random swimming trajectories are observed on the static surface without any specific directionality in the bacterial swimming patterns [Fig. 5A (i) and movie S3]. In contrast, *E. coli* cells exhibit unidirectional traces on the dynamic surface aligned with the propagation direction of the undulatory topographical waves [Fig. 5A (ii) and movie S4]. During the real-time optical imaging

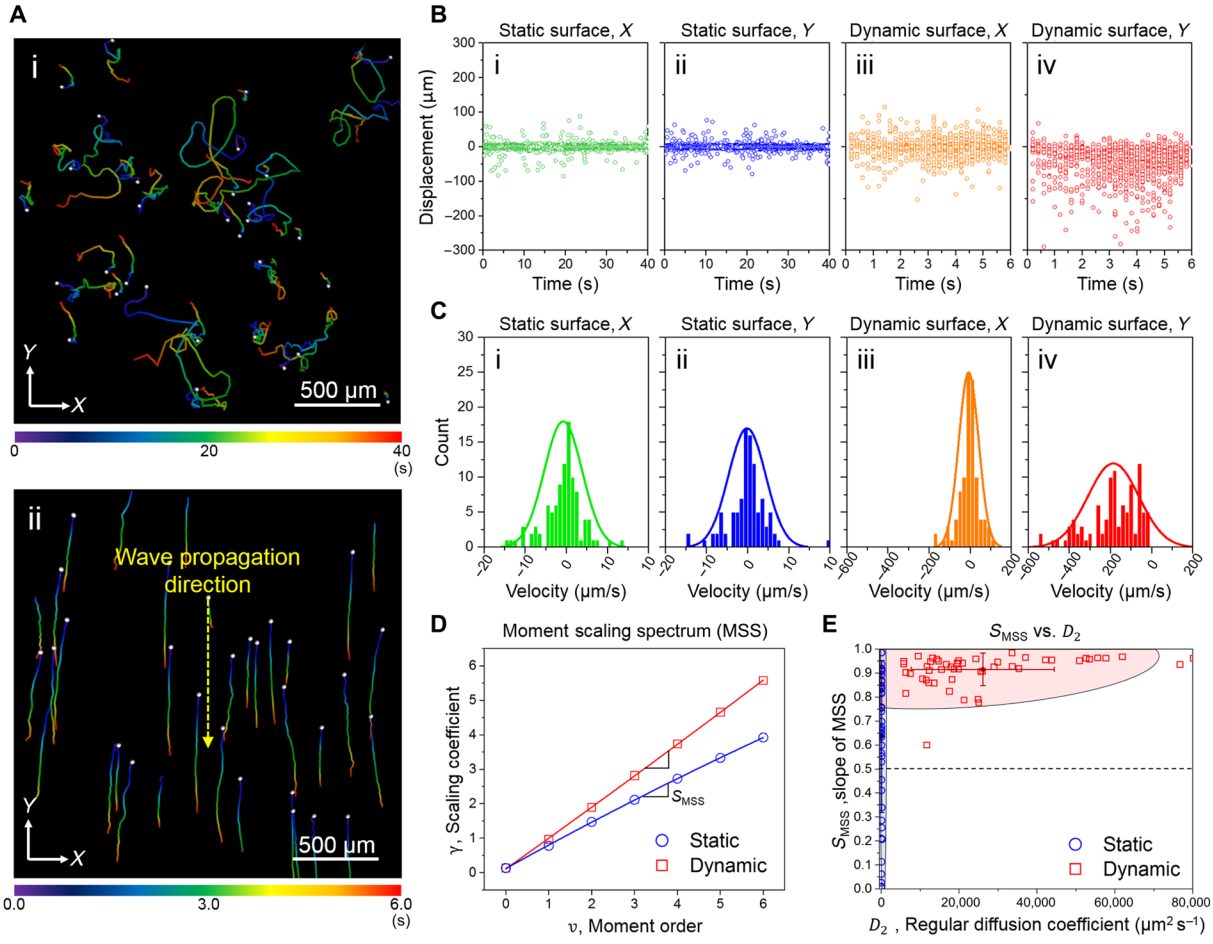

Fig. 5. Analysis of trajectories of bacterial cells on the dynamic undulatory composite. (**A**) Trajectories of *E. coli* on the (i) static surface and (ii) dynamic undulatory surface. Axes for the two-dimensional observation plane and time legends are noted. (**B**) *X* and *Y* displacements of *E. coli* cells on the (i and ii) static and (iii and iv) dynamic surfaces. (**C**) Velocity histogram of *E. coli* cells on the (i and ii) static and (iii and iv) dynamic surfaces. (**D**) Moment scaling spectrum (MSS) of representative bacterial trajectories on the static and dynamic surfaces. (**E**) S_{MSS}/D_2 scatter of *E. coli* trajectories on the static and dynamic surfaces.

experiments, the reciprocating movement of the magnet was maintained at a relatively low speed of 0.5 mm s^{-1} to track the bacterial trajectories with an optical microscope and particle-tracking software.

To quantify the bacterial movements on the undulatory composite and static control surfaces, the *X*- and *Y*-directional displacements of the cells for each surface are depicted as a function of the time elapsed (Fig. 5B). The displacements of bacterial cells on the static surface are relatively small and within ±100 μm in both the *x* and *y* directions over the tested time span of 40 s (Fig. 5B, i and ii). The *X* displacements of bacteria on the dynamic surface are also not remarkable (Fig. 5B, iii). However, the *Y* displacements on the dynamic surface are immensely scattered compared to those on the static surface or the *X* displacements on the dynamic surface (Fig. 5B, iv). This results from the topographical wave–induced fluid flow in the reciprocating direction (*y*) of the magnet, as demonstrated by the PIV results (Fig. 4). Accordingly, bacterial cells on the dynamic surface move with a large velocity (~200 μm s^{-1}) in the *y* direction, while the cells on the static surface have a relatively low velocity, both in the *x* and *y* directions (Fig. 5C). Quantitative comparisons of the displacements of individual bacterial cells with respect to the wave propagation vectors show that the moving directions of bacterial cells are highly consistent with the propagating direction of the waves (fig. S5A).

We classified the different bacterial movements on the static and dynamic surfaces by adopting the moment scaling spectrum (MSS) theory. Traces of dispersive particles can be quantified using this theory by calculating the moments of the displacements of individual particles (*35*). In the MSS theory, each moment $\mu_\nu(\delta t)$ is assumed to vary according to a power law of the time shift (δt), $\mu_\nu(\delta t) \propto \delta t^{\gamma\nu}$. Using linear least-squares regression to log $\mu_\nu(\delta t)$ versus log δt, scaling coefficient γ_ν can be determined for each moment order ν. The diffusion coefficient (D_ν) can be obtained from the *y*-axis intercept. The plot of γ_ν versus ν is called the MSS, and the slope of the MSS (S_{MSS}) is used as a criterion to distinguish between the dynamic modes of dispersive particles. S_{MSS} values ranging from 0 to 0.5 correspond to subdiffusion, while those from 0.5 to 1 correspond to superdiffusion. A detailed description of the MSS theory is available in Materials and Methods. As shown in Fig. 5D, *E. coli* cells on both the static and dynamic undulatory surfaces belong to the superdiffusion mode. However, bacterial cells on each surface exhibit distinguished modes of movements. The averaged S_{MSS} value and diffusion coefficient D_ν of bacterial cells on the static surface are 0.63 and 25.3 μm^2 s^{-1}, respectively. However, on the dynamic undulatory composite surface, the averaged S_{MSS} (0.91) and *D* values (26,000 μm^2 s^{-1}) are significantly higher (Fig. 5E and fig. S5B). This result confirms that

the undulatory topographical waves induce noticeable directional fluid flows and therefore enable the sweeping of planktonic bacterial cells.

To further investigate the antifouling performance of the proposed undulatory composite surface, we cultured *E. coli* cells on the static and dynamic surfaces with topographical waves of different time scales (*T*: 3, 20, and 60 s) and different length scales (*H*: 0.176, 0.312, and 0.394 mm) for 18 hours (Fig. 6). The undulatory dynamic surfaces exhibited largely enhanced biofilm resistance compared to that of the static surface (Fig. 6, A and B). Figure 6B is a phase diagram displaying a summary of the biofilm resistance of the dynamic surfaces according to the values of *T* and *H*. The combined condition of time scale *T* smaller than 3 s and length scale *H* higher than 0.394 mm exhibits outstanding antifouling performance with the undulatory surface waves without any surface chemical modification or fabrication of nanostructures. Even the dynamic surface with a relatively low wave speed (high *T*) is more effective in the prevention of biofilm formation compared to the static surface. For example, the area of bacterial coverage on the dynamic surface with *H* of 0.394 mm and *T* of 60 s is approximately 37.2% lower than that of the static surface. With the decrease of *T*, the area of bacterial coverage is remarkably reduced (Fig. 6C). The areas of bacterial coverage on the dynamic surfaces with *T* values of 20 and 3 s are 77.5 and 91.2% lower than that on the static surface (for *H* of 0.394 mm). This is because for a fixed *H* value, a smaller *T* leads to a higher vorticity and larger wall shear stresses (fig. S6). According to previous studies, at a high flow rate, the hydrodynamic boundary layer formed close to the surface decreases (*18*, *36*). Therefore, bacterial cells near the surface are subjected to high shear (fig. S6B) (*37*). In addition, planktonic bacterial cells that swim at a higher flow rate have a lower chance of coming into contact with the surface. Accordingly, bacteria under such a high shear rate cannot form a proper biofilm (*37*, *38*). This agrees with our observations in the present study (Figs. 5 and 6). For a fixed *T*, the dimple depth *H* also has an influence on the antifouling performance. Higher *H* values lead to better fouling resistance. This

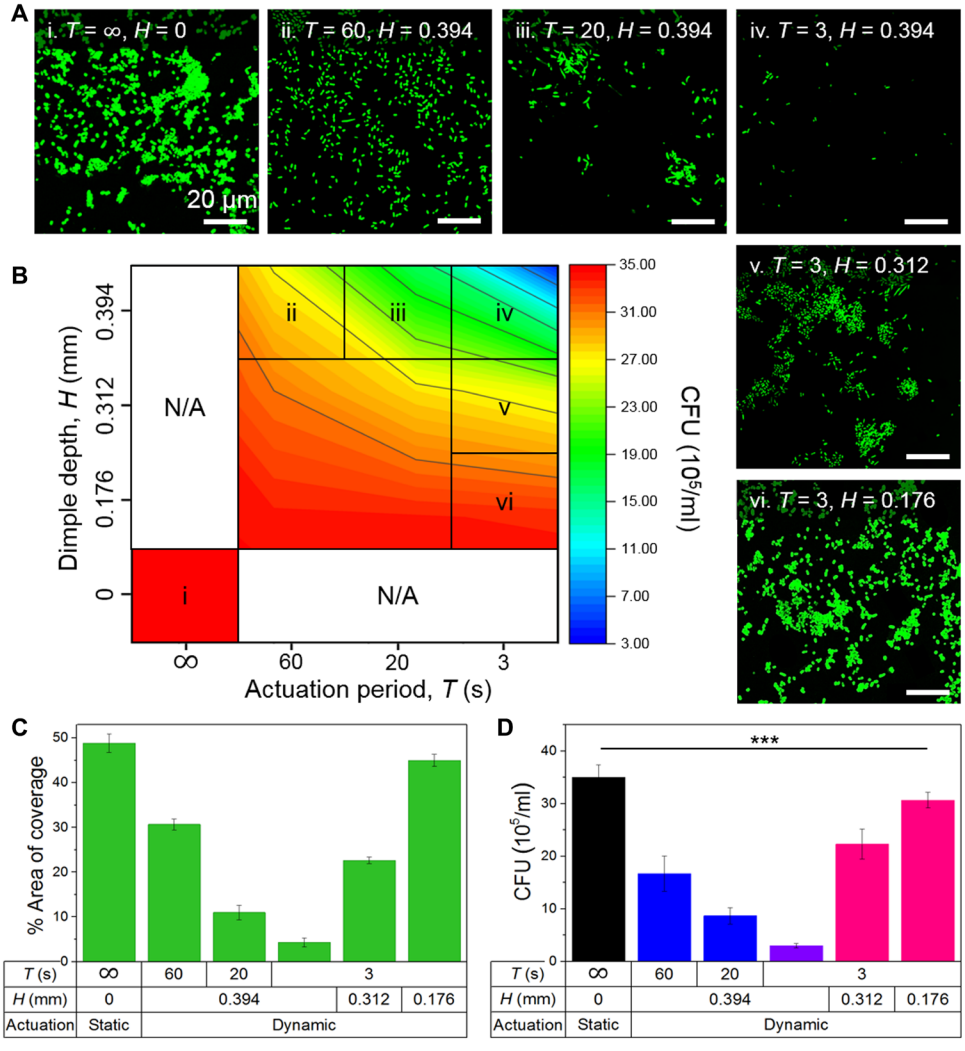

Fig. 6. Anti-biofilm assay. (**A**) Confocal microscopy images of the stained *E. coli* cultured (18 hours at 37°C) on the static control and dynamic undulatory composite surfaces with different operation conditions (*T* and *H*) of topographical waves: (i) $T = \infty$ and $H = 0$, (ii) $T = 60$ s and $H = 0.394$ mm, (iii) $T = 20$ s and $H = 0.394$ mm, (iv) $T = 3$ s and $H = 0.394$ mm, (v) $T = 3$ s and $H = 0.312$ mm, and (vi) $T = 3$ s and $H = 0.176$ mm. (**B**) Phase diagram showing different regimes of the CFU counting according to the actuation period (*T*) and dimple depth (*H*) of topographical waves. (**C**) Areal coverages of the live *E. coli* cultured on the different static and dynamic surfaces. (**D**) CFUs of the *E. coli* cultured on the different static and dynamic surfaces ($n = 5$; $^{***}P < 0.001$; data were analyzed by Kruskal-Wallis' *H* test).

implies that sufficient deformation of the bottom surface (but less than ~0.4 mm) is required to induce great vortices and larger wall shear stress to prevent bacterial attachment (fig. S6, A and B). The analysis of colony-forming units (CFUs) on the static and dynamic surfaces shows overall similar trends with the results of the area coverage analysis (Fig. 6D).

As briefly described, nanostructures or chemical moieties could be added over the s-PUA skin layer of the undulatory composite (fig. S7A, i to iv). Previous studies reported that nanostructures with sharp tips can induce lysis of bacterial cells while physically rupturing the cell membrane (*6*, *39*). Thus, they are effective for the prevention of biofilm formation. MPC is a well-known effective antifouling material (*4*, *39*). By generating a nanoscale needle array or coating of the antifouling polymer MPC over the skin layer, the biofilm resistance of the dynamic composite can be further enhanced for the same T and H values (fig. S7B). However, the dynamic surface with proper period and depth of waves (e.g., T = 3 s and H = 0.394 mm) exhibits outstanding anti-biofilm performance that is superior to that of the static surface with nanoneedles or MPC grafting (fig. S7, C and D). This result confirms that the undulatory dynamic composite proposed in this study could serve as an effective antifouling material with high performance.

DISCUSSION

In summary, we proposed a bioinspired antifouling strategy that can prevent surface fouling based on deliberate induction of strong vortices and high shear flows using undulatory topographical waves of the responsive dynamic composite. The PIV measurement, FEA, and real-time tracking of bacterial cells show that the undulatory surface waves induce local and global vortices over the dynamic composite, fundamentally inhibiting the attachment of foulants to the surface. Accordingly, the dynamic composite exhibits outstanding antifouling performance against *E. coli* with the simple topographical motion without surface modification with chemicals or nanostructures. According to previous studies, shear stress alone cannot induce enough resistance to biofilm formation (*38*, *40*). On the basis of our experimental and simulation results shown in Fig. 4 and figs. S4 and S6, the local and global vortices together with the oscillatory shear flow on the undulatory surface are all responsible for the enhanced antifouling performance of the dynamic undulatory composite. Although we use a magnetic field–based actuation in this study to drive the surface undulations, passive mechanisms that can generate undulatory surface waves by external flow or other environmental forces can be harnessed to devise dynamic antifouling surfaces with broader applicability. With the highly fluctuating flow-based outstanding antifouling property, the dynamic composite with coordinated undulatory topographical waves could contribute to the development of a new-concept bioinspired dynamic and sustainable antifouling strategy.

MATERIALS AND METHODS

Fabrication of the responsive dynamic undulatory composite

First, the PDMS prepolymer (SYLGARD 184, Dow Corning Korea, Republic of Korea), PDMS curing agent, and silicone oil (O02-543-666, LK Lab Korea, Republic of Korea) were mixed together in a 50:1:10 weight ratio. The mixture solution was drop-casted over a supporting glass or PET substrate, followed by thermal curing at 70°C for 2 hours. This generated the RDL over the supporting layer. The amount of the mixture was controlled so that the final thickness of the damping layer was in the range of 0.7 to 2.1 mm. For the formation of the magnetic muscle layer over the damper, the PDMS prepolymer, curing agent, and CI particle (diameter, 1 to 5 μm; C3518, Sigma-Aldrich Korea, Republic of Korea) were mixed together in a 100:1.5:150 weight ratio. Then, the mixture was drop-casted over the damping layer, followed by baking at 70°C for 2 hours. The thickness of the muscle layer was controlled by modulating the casting amount of the mixture solution. Subsequently, the surface of the magnetic muscle was treated with oxygen plasma [60 standard cubic centimeters per minute (sccm), 100 W, and 1 min]. A drop of the s-PUA prepolymer was spin-coated over the muscle layer, followed by UV curing (λ = 250 to 400 nm; dose, 300 mJ cm^{-2}). During the photopolymerization process, the surface of the s-PUA was covered with a PET film, which was removed after the UV curing.

Control of the undulatory topographical waves of the dynamic composite

A spherical neodymium magnet (diameter, 10 mm; magnetic flux density, ~0.5 T; JL Magnet, Republic of Korea) was fixed on a linear actuator (mightyZAP, IRROBOT, Republic of Korea). The fabricated dynamic composite was placed just above the magnet. The horizontal translation of the magnet attached to the linear actuator gave rise to undulatory topographical waves of the dynamic composite. The frequency of the undulatory waves was controlled by modulating the speed of the actuator. Undulatory motion of the dynamic composite was observed with a stereo zoom microscope (Axio Zoom V16, Zeiss, Germany). To obtain time-lapse fluorescence images of the dynamic motions, rhodamine B (87180-1510, JUNSEI, Japan) was added to the s-PUA prepolymer during the fabrication process of the skin layer.

Particle image velocimetry

A part of the wall of a dish containing the dynamic undulatory composite was cut and sealed with a transparent cover glass to avoid the optical distortion caused by the curved wall. Fluorescence particles (PMMA-Rhodamine B-particle, microParticles GmbH, Germany) were seeded into working fluid as tracers. The average diameter and density of the tracer particles were approximately 20 to 50 μm and 1.19 g/ml, respectively. NaCl solution with a density of 1.19 g/ml was used as the working fluid to avoid sedimentation of the tracer particles. To minimize the effect of a free surface on the flow motion, the free surface of the working fluid was located 4 mm above the skin layer. Velocity fields in two different measurement planes were obtained to verify the effect of the dynamic behavior of the surface on the flow at different locations. Plane 1 was set parallel to the magnet movement and passed through the center of the dynamic surface. Plane 2 was perpendicular to plane 1 and also passed through the center of the dynamic surface. Each measurement plane was illuminated with a 0.5-mm-thin laser light sheet, which was formed by a 50-mW continuous solid-state laser (MSL-III-532-50mW, UNIOTECH, Republic of Korea). A high-speed camera (FASTCAM Mini UX100, Photron, Japan) with a macro-lens attached (AF Micro NIKKOR 105 mm) was used to capture consecutive images. The effective pixel size of the camera was 17 μm. During 10 periods of magnet movements, consecutive images were captured at a frame rate of 125 frames per second with an exposure time of 1/500 s. Instantaneous velocity field information was obtained by applying

the PIVview software (PIVview 2C, PIVTEC, Germany) to the captured particle images. The interrogation window size was 32 × 32 pixels with 50% overlapping. The phase-averaged velocity field according to the phase angle of the undulatory waves was used to analyze the periodic variation of the flow structure around the dynamic composite.

Real-time analysis of bacterial trajectories

For real-time optical imaging, *E. coli* culture [optical density at 600 nm (OD_{600}) = 0.001] was inoculated on the static and dynamic composite surfaces. During the optical imaging experiment, the reciprocating speed of the magnet was maintained at a relatively low speed of 0.5 mm s^{-1}. Traces of *E. coli* cells were then monitored using a stereo zoom microscope (Axio Zoom V16, Zeiss, Germany) and recorded with a microscope-mounted camera (iXon EMCCD, Andor Technology–Oxford Instruments, England). The trajectories and the positional information of *E. coli* were analyzed and extracted using a particle-tracking software (Imaris, Bitplane, Switzerland).

The mean moment of displacement of order v (μ_v) was calculated using a customized MATLAB (R2019a; MathWorks, USA) routine based on the following equation

$$\mu_v(\Delta n) = \frac{1}{M_l - \Delta n} \sum_{n=0}^{M_l - \Delta n - 1} |x_l(n + \Delta n) - x_l(n)|^{\nu}$$

where $x_l(n)$ is the position vector on the trajectory l with the total number of traced points M_l at time $n\Delta t$ for $n = 0, 1, 2, \ldots, M_l - 1$. To define the diffusion mode, μ_v was calculated for $\Delta n = 1, 2, \ldots, M_l/3$ and plotted versus time shift $\delta t = \Delta n \Delta t$ in a logarithmic plot. For different orders of $v = 0, 1, 2, \ldots, 6$, the slope (γ_v) of the plot log $\mu_v(\delta t)$ versus log δt was determined using a linear least-square regression method. The plot of γ_v versus v corresponds to the MSS. Here, each moment of the displacement was assumed to depend on the time shift in a power law of $\mu_v(\delta t) \propto \delta t^{\gamma v}$. The diffusion mode can be classified on the basis of the criteria; pure diffusion for $S_{MSS} = 1/2$, superdiffusion for $S_{MSS} > 1/2$, and subdiffusion for $S_{MSS} < 1/2$. Moreover, the diffusion coefficients (D_v) of the orders ($v = 0, 1, 2, \ldots, 6$) were determined using the following equation

$$D_v = (\mathrm{dv})^{-1} e^{y_0}$$

where y_0 is the y-axis intercept of the plot log $\mu_v(\delta t)$ versus log δt. Among the diffusion coefficients of different orders, D_2 corresponds to the regular diffusion coefficient. The scatter plot S_{MSS} versus D_2 showed the 50 representative trajectories with respect to S_{MSS} and D_2, which provide rich information about diffusion behaviors.

Anti-biofilm assay

To obtain the anti-biofilm assay, *E. coli* (ATCC25404, American Type Culture Collection, USA) was cultured in 5 ml of LB (LB Broth Miller, BD Difco, USA) using a shaking incubator (VS-8480, Vision Scientific, Daejeon, Republic of Korea) at 200 rpm and 37°C overnight. The cultured bacterial concentration was measured using a spectrophotometer (GENESYS 20, Thermo Fisher Scientific, USA) at a wavelength of 600 nm (OD_{600}) to obtain an OD of 0.3. Subsequently suspended culture medium was separated by centrifuge (5910R, Eppendorf, Germany) at 5000 rpm for 10 min and replaced with fresh culture medium to supply enough nutrients to the bacteria. The obtained bacteria were cultured for 2 hours at 37°C, and the concentration was adjusted to OD_{600} of 0.1. Then, the dynamic composite specimens were sterilized with 70% ethanol and 1-min UV exposure and were then immersed in the bacterial suspension followed by incubation for 18 hours at 37°C. During the incubation, the surface of the composite specimens was undulated with controlled wave depths and periods using a permanent magnet installed on a linear actuator. To quantify the areal coverage and CFU assay, specimens were prepared in multiple sets and incubated simultaneously. After the incubation process, specimens were rinsed with phosphate-buffered saline (PBS) three times and then placed in 24-well plates of 1 cm × 1 cm physical dimension. Those were then stained using a fluorescent labeling reagent (BacLight, L7012, Invitrogen, USA) to examine bacterial viability. The stained specimens were kept in a dark environment at room temperature for 15 min and rinsed three times with PBS solution. The specimens were monitored with a multiphoton confocal microscope (LSM 780 Configuration 16 NLO, Zeiss, Germany), and subsequently, the areal coverage of the stained bacteria was analyzed using ImageJ software (National Institutes of Health, Bethesda, MD). For the CFU assay, the PBS-rinsed specimens were transferred to a falcon tube with 1 ml of sterile PBS and vortexed for 5 min to remove all bacteria from the specimen's surface. Serially diluted bacterial solution was plated on LB agar surface and incubated for 18 hours; then, the grown bacteria were counted to quantify the CFUs.

Finite element analysis

FEA was conducted for the analysis of interactions between the magnetic field distribution, structural deformation, and fluid behavior (velocity field, particle trajectory, and vorticity), using multiphysics analysis (COMSOL Multiphysics 5.3a, COMSOL Inc., Sweden). The dynamic undulatory topographical waves and wave propagation phenomena were modeled with parameters (t_{RDL}, H, and T) and experimentally obtained physical properties. More than 800,000 free triangular elements (minimum element quality ~ 0.67 out of 1.0) were used for the mesh refinement in the numerical analysis.

Statistical analysis

Mann-Whitney's U test was performed to compare two different conditions (fig. S8D). To compare three or more conditions, Kruskal-Wallis' H test was conducted (Fig. 6D and fig. S7). In all cases, values of $P < 0.05$ were considered statistically significant.

SUPPLEMENTARY MATERIALS

Supplementary material for this article is available at http://advances.sciencemag.org/cgi/content/full/5/11/eaax8935/DC1

Note S1. Theory for magnetic field–induced structural deformations of the magnetoresponsive material

Note S2. Theory for structure deformation–induced fluid field (fluid-structure interactions)

Note S3. Characterization of the flow over the undulatory surface

Fig. S1. A schematic showing the experiment setup together with geometries of the dynamic undulatory composite.

Fig. S2. FEA for the dynamic undulatory wave under a controlled magnetic field.

Fig. S3. A schematic illustration describing the terms of depth (*H*) and period (*T*) of the topographical wave.

Fig. S4. FEA of the fluid velocity field and the path lines on the dynamic undulatory composite.

Fig. S5. Quantitative analysis of bacterial trajectories on the dynamic undulatory composite.

Fig. S6. FEA of the fluid flow on the dynamic undulatory composite with different wave depth (*H*) and period (*T*).

Fig. S7. Anti-biofilm assays for four different types of surfaces under various static and dynamic conditions.

Movie S1. Real-time monochromic video recording of undulatory surface waves of the composite generated by the translation of a permanent magnet.

Movie S2. Real-time fluorescence video recording of undulatory surface waves of the composite generated by the translation of a permanent magnet.

Movie S3. Real-time video recording of traced *E. coli* on the static control surface.
Movie S4. Real-time video recording of traced *E. coli* on the dynamic undulatory surface.

REFERENCES AND NOTES

1. K. Baek, J. Liang, W. T. Lim, H. Zhao, D. H. Kim, H. Kong, In situ assembly of antifouling/bacterial silver nanoparticle-hydrogel composites with controlled particle release and matrix softening. *ACS Appl. Mater. Interfaces* **7**, 15359–15367 (2015).
2. D. O. Schairer, J. S. Chouake, J. D. Nosanchuk, A. J. Friedman, The potential of nitric oxide releasing therapies as antimicrobial agents. *Virulence* **3**, 271–279 (2012).
3. C. M. Magin, S. P. Cooper, A. B. Brennan, Non-toxic antifouling strategies. *Mater. Today* **13**, 36–44 (2010).
4. K. Ishihara, T. Ueda, N. Nakabayashi, Preparation of phospholipid polylners and their properties as polymer hydrogel membranes. *Polym. J.* **22**, 355–360 (1990).
5. L. Jiang, Y. Zhao, J. Zhai, A lotus-leaf-like superhydrophobic surface: A porous microsphere/nanofiber composite film prepared by electrohydrodynamics. *Angew. Chem. Int. Ed.* **43**, 4338–4341 (2004).
6. C. M. Bhadra, V. K. Truong, V. T. Pham, M. Al Kobaisi, G. Seniutinas, J. Y. Wang, S. Juodkazis, R. J. Crawford, E. P. Ivanova, Antibacterial titanium nano-patterned arrays inspired by dragonfly wings. *Sci. Rep.* **5**, 16817 (2015).
7. A. K. Epstein, T.-S. Wong, R. A. Belisle, E. M. Boggs, J. Aizenberg, Liquid-infused structured surfaces with exceptional anti-biofouling performance. *Proc. Natl. Acad. Sci. U.S.A.* **109**, 13182–13187 (2012).
8. J. F. Schumacher, C. J. Long, M. E. Callow, J. A. Finlay, J. A. Callow, A. B. Brennan, Engineered nanoforce gradients for inhibition of settlement (attachment) of swimming algal spores. *Langmuir* **24**, 4931–4937 (2008).
9. K.-C. Park, H. J. Choi, C.-H. Chang, R. E. Cohen, G. H. McKinley, G. Barbastathis, Nanotextured silica surfaces with robust superhydrophobicity and omnidirectional broadband supertransmissivity. *ACS Nano* **6**, 3789–3799 (2012).
10. Y. Rahmawan, L. Xu, S. Yang, Self-assembly of nanostructures towards transparent, superhydrophobic surfaces. *J. Mater. Chem. A* **1**, 2955–2969 (2013).
11. C. Hao, J. Li, Y. Liu, X. Zhou, Y. Liu, R. Liu, L. Che, W. Zhou, D. Sun, L. Li, Superhydrophobic-like tunable droplet bouncing on slippery liquid interfaces. *Nat. Commun.* **6**, 7986 (2015).
12. J. H. Kim, S. M. Kang, B. J. Lee, H. Ko, W.-G. Bae, K. Y. Suh, M. K. Kwak, H. E. Jeong, Remote manipulation of droplets on a flexible magnetically responsive film. *Sci. Rep.* **5**, 17843 (2015).
13. S.-H. Lee, M. Seong, M. K. Kwak, H. Ko, M. Kang, H. W. Park, S. M. Kang, H. E. Jeong, Tunable multimodal drop bouncing dynamics and anti-icing performance of a magnetically responsive hair array. *ACS Nano* **12**, 10693–10702 (2018).
14. C. M. Kirschner, A. B. Brennan, Bio-inspired antifouling strategies. *Annu. Rev. Mater. Res.* **42**, 211–229 (2012).
15. L. Pocivavsek, J. Pugar, R. O'Dea, S.-H. Ye, W. Wagner, E. Tzeng, S. Velankar, E. Cerda, Topography-driven surface renewal. *Nat. Phys.* **14**, 948–953 (2018).
16. L. Pocivavsek, S. H. Ye, J. Pugar, E. Tzeng, E. Cerda, S. Velankar, W. R. Wagner, Active wrinkles to drive self-cleaning: A strategy for anti-thrombotic surfaces for vascular grafts. *Biomaterials* **192**, 226–234 (2019).
17. A. Tripathi, H. Shum, A. C. Balazs, Fluid-driven motion of passive cilia enables the layer to expel sticky particles. *Soft Matter* **10**, 1416–1427 (2014).
18. C. Berne, C. K. Ellison, A. Ducret, Y. V. Brun, Bacterial adhesion at the single-cell level. *Nat. Rev. Microbiol.* **16**, 616–627 (2018).
19. Y. Yawata, J. Nguyen, R. Stocker, R. Rusconi, Microfluidic studies of biofilm formation in dynamic environments. *J. Bacteriol.* **198**, 2589–2595 (2016).
20. A. K. Epstein, D. Hong, P. Kim, J. Aizenberg, Biofilm attachment reduction on bioinspired, dynamic, micro-wrinkling surfaces. *New J. Phys.* **15**, 095018 (2013).
21. S.-J. Park, M. Gazzola, K. S. Park, S. Park, V. Di Santo, E. L. Blevins, J. U. Lind, P. H. Campbell, S. Dauth, A. K. Capulli, Phototactic guidance of a tissue-engineered soft-robotic ray. *Science* **353**, 158–162 (2016).
22. R. G. Bottom Ii, I. Borazjani, E. L. Blevins, G. V. Lauder, Hydrodynamics of swimming in stingrays: Numerical simulations and the role of the leading-edge vortex. *J. Fluid Mech.* **788**, 407–443 (2016).
23. H. E. Jeong, J.-K. Lee, H. N. Kim, S. H. Moon, K. Y. Suh, A nontransferring dry adhesive with hierarchical polymer nanohairs. *Proc. Natl. Acad. Sci. U.S.A.* **106**, 5639–5644 (2009).
24. A. Dorfmann, R. Ogden, Magnetoelastic modelling of elastomers. *Eur. J. Mech. A. Solids* **22**, 497–507 (2003).
25. I. Brigadnov, A. Dorfmann, Mathematical modeling of magneto-sensitive elastomers. *Int. J. Solids Struct.* **40**, 4659–4674 (2003).
26. D. J. Griffiths, *Introduction to Electrodynamics* (Prentice Hall, 1962).
27. J. Rychlewski, On Hooke's law. *J. Appl. Math. Mech.* **48**, 303–314 (1984).
28. G. Sandberg, P.-A. Wernberg, P. Davidsson, *Computational Aspects of Structural Acoustics and Vibration* (Springer, 2008), pp. 23–101.
29. E. Uddin, H. J. Sung, Simulation of flow-flexible body interactions with large deformation. *Int. J. Numer. Methods Fluids* **70**, 1089–1102 (2011).
30. F. B. Tian, H. Dai, H. Luo, J. F. Doyle, B. Rousseau, Fluid-structure interaction involving large deformations: 3D simulations and applications to biological systems. *J. Comput. Phys.* **258**, 451–469 (2014).
31. G. Hou, J. Wang, A. Layton, Numerical methods for fluid-structure interaction—A review. *Commun. Comput. Phys.* **12**, 337–377 (2012).
32. S. Basting, A. Quaini, S. Čanić, R. Glowinski, Extended ALE method for fluid–structure interaction problems with large structural displacements. *J. Comput. Phys.* **331**, 312–336 (2017).
33. S. Kim, W.-X. Huang, H. J. Sung, Constructive and destructive interaction modes between two tandem flexible flags in viscous flow. *J. Fluid Mech.* **661**, 511–521 (2010).
34. A. Seena, H. J. Sung, Dynamic mode decomposition of turbulent cavity flows for self-sustained oscillations. *Int. J. Heat Fluid Flow* **32**, 1098–1110 (2011).
35. H. E. Jeong, I. Kim, P. Karam, H. J. Choi, P. Yang, Bacterial recognition of silicon nanowire arrays. *Nano Lett.* **13**, 2864–2869 (2013).
36. H. Schlichting, K. Gersten, *Boundary-Layer Theory* (Springer, 2016).
37. M. K. Kim, F. Ingremeau, A. Zhao, B. L. Bassler, H. A. Stone, Local and global consequences of flow on bacterial quorum sensing. *Nat. Microbiol.* **1**, 15005 (2016).
38. R. Hartmann, P. K. Singh, P. Pearce, R. Mok, B. Song, F. Díaz-Pascual, J. Dunkel, K. Drescher, Emergence of three-dimensional order and structure in growing biofilms. *Nat. Phys.* **15**, 251–256 (2018).
39. H.-H. Park, K. Sun, M. Seong, M. Kang, S. Park, S. Hong, H. Jung, J. Jang, J. Kim, H. E. Jeong, Lipid-hydrogel-nanostructure hybrids as robust biofilm-resistant polymeric materials. *ACS Macro Lett.* **8**, 64–69 (2018).
40. R. Rusconi, J. S. Guasto, R. Stocker, Bacterial transport suppressed by fluid shear. *Nat. Phys.* **10**, 212–217 (2014).

Acknowledgments: We dedicate this work to the late K.-Y. Suh who was a mentor to us. We express gratitude for access to the supercomputing resources of the UNIST Supercomputing Center. **Funding:** This work was supported by the National Research Foundation of Korea (NRF) (2019M3C1B7025092). **Author contributions:** H.K. and H.-H.P. performed the experiments and wrote the manuscript. H.B. performed the PIV tests and analysis of the experimental results. M.K. assisted with the experiments. J.R. and H.J.S. consulted on the theoretical and numerical analysis of the experimental results. S.J.L. consulted on the experiments, analyzed the experimental results, and wrote the manuscript. H.E.J. conceived and supervised the research and also wrote the manuscript. **Competing interests:** The authors declare that they have no competing interests. **Data and materials availability:** All data needed to evaluate the conclusions in the paper are present in the paper and/or the Supplementary Materials. All data related to this paper may be requested from the authors.

Submitted 2 May 2019
Accepted 4 October 2019
Published 29 November 2019
10.1126/sciadv.aax8935

Citation: H. Ko, H.-H. Park, H. Byeon, M. Kang, J. Ryu, H. J. Sung, S. J. Lee, H. E. Jeong, Undulatory topographical waves for flow-induced foulant sweeping. *Sci. Adv.* **5**, eaax8935 (2019).

Science Advances

Undulatory topographical waves for flow-induced foulant sweeping

Hangil Ko, Hyun-Ha Park, Hyeokjun Byeon, Minsu Kang, Jaeha Ryu, Hyung Jin Sung, Sang Joon Lee and Hoon Eui Jeong

Sci Adv **5** (11), eaax8935.
DOI: 10.1126/sciadv.aax8935